Rayleigh wave group velocity dispersion tomography of West Africa using regional earthquakes and ambient seismic noise

Yacouba Ouattara, Dimitri Zigone, Alessia Maggi

Journal of Seismology manuscript No.
(will be inserted by the editor)

Rayleigh wave group velocity dispersion tomography of West-Africa using regional earthquakes and ambient seismic noise

Yacouba Ouattara · Dimitri Zigone · Alessia Maggi

Received: date / Accepted: date

Abstract West Africa could teach us much about the early tectonic history of Earth, but current seismic models of the regional crustal and lithospheric structure lack the resolution required to answer all but the most basic research questions. We have improved the resolution of group-velocity maps of the West African craton by complementing the uneven path distribution of earthquake-generated surface-waves with surface-waves reconstructed from ambient noise cross-correlations. Our joint dataset provides good spatial coverage of group-velocity measurements from 20 to 100 s period, enabling us to reduce artefacts in our group-velocity maps and improve their resolution. Our maps correlate well with regional geological features. At short periods, they highlight differences in crustal thickness, recent tectonic activity, and thick sediments. At long periods, we found lower velocities due to hot, thin lithosphere under the Pan-African mobile belt and faster velocities due to cold, thick lithosphere under the Man-Leo and Reguibat shields. Our higher resolution maps advance us a step towards revealing the detailed lithospheric structure and tectonic processes of West Africa.

Keywords West Africa craton · Rayleigh waves · dispersion · cross-correlation · ambient noise · group velocity

Y. Ouattara
Institut de Physique du Globe de Strasbourg, Ecole et Observatoire des Sciences de la Terre, Strasbourg University/CNRS, Strasbourg, France.

Université Felix Houphouët-Boigny/Abidjan, UFR des Sciences de la Terre et des Ressources Minières, Laboratoire de Géophysique Appliquée, Station Géophysique de Lamto, Côte d'Ivoire.

E-mail: yb.ouattara@gmail.com

D. Zigone · A. Maggi
Institut de Physique du Globe de Strasbourg, Ecole et Observatoire des Sciences de la Terre, Strasbourg University/CNRS, Strasbourg, France

1 Introduction

Over the past 30 years, seismologists have exploited the frequency dependence of surface-wave velocities to investigate Earth structure and construct seismic velocity maps whose resolution improves as the quantity of data increases (Ritzwoller et al., 2001; Ritzwoller and Levshin, 1998; Romanowicz, 2003). These maps have helped us understand how the crust and the mantle interact (Yao et al., 2010; Shen et al., 2013; Yao et al., 2008), how tectonic processes and fault systems evolve over time (Ben-Zion, 2008; Becker, 2012; Shen and Ritzwoller, 2016), and even how the solid Earth reacts to changes in rainfall (Chanard et al., 2014; Craig et al., 2017).

For the West African craton, we only have moderate to low-resolution surface-wave velocity maps derived from global-scale studies, because large parts of the region are aseismic and the distribution of broad-band seismic stations has long been sparse (Fairhead and Reeves, 1977; Hadiouche and Jobert, 1988; Hadiouche et al., 1989; Dorbath and Montagner, 1983; Ritsema and van Heijst, 2000; Hazler et al., 2001; Pasyanos et al., 2001; Sebai et al., 2006; Pasyanos and Nyblade, 2007; Gangopadhyay et al., 2007; Priestley et al., 2008). Despite their low resolution, these studies all show similar, robust features: fast velocities beneath the cratonic areas; slow velocities in active orogenic regions, rift systems, and large sedimentary basins. More recent surface wave global tomography studies show similar features with slightly higher resolution (Pasyanos et al., 2014; Ma et al., 2014) but only analyse periods longer than 30s, which limits their sensitivity to the upper crust.

Higher resolution seismic images of the West African craton would enable us to answer many pending research questions about the region. For example: How did the structures created by the earliest geological processes influence later plate tectonics (Binks and Fairhead, 1992)? What lateral density and viscosity variations should we include in regional models of lithospheric rebound (Bills et al., 2007)? Better models of the crust and upper mantle might also help us locate and discriminate small, local, or regional seismic events, whose travel times are affected by strong lateral heterogeneities (Villasenor et al., 2001).

We plan to improve the resolution of seismic models of the West African craton by increasing the density of surface-wave measurements within the region. In this paper, we complement the patchy and uneven path distribution that can be obtained from measurements of earthquake-generated surface-waves by making similar measurements on surface-waves reconstructed from ambient noise cross-correlations (e.g. Shapiro and Campillo, 2004; Shapiro et al., 2005; Zigone et al., 2015). The correlation approach exploits the ubiquitous nature of ambient seismic noise and opens up low seismicity regions to tomographic imaging (e.g. Poli et al., 2012). Such combined earthquake and seismic noise approaches have been applied before (e.g. Yang et al., 2008a,b) but not, we believe, to the West African craton.

2 Geological context of the West African craton

The African continent bears imprints of tectonic episodes that occurred from the Archean to the present day. After the Archean nucleis stabilized around 2.5 Ga, the Kibarian orogenesis (1.37-1.31 Ga) separated the single, stable craton into the Kalahari, Congo and West Africa cratons (Djomani, 1993). At the end of the Pan-African orogenic episode, the African continent was composed of stable cratons with thick lithosphere surrounded by orogenic belts with thick crust but thin lithosphere.

Today, the geology of West Africa is dominated by the West African craton, which is largely covered by the Neoproterozoic to Paleozoic Taoudeni basin (Figure 1). Archean rocks are exposed in the Reguibat shield to the north and the Man-Leo shield to the south. Strong similarities between them suggest that the shields are part of a larger craton that underlies the Basin (Begg et al., 2009). A series of Pan-African and Hercynian belts rings the West African craton: the Pharusian and Dahomeyides belts are regions of nappes along the eastern margin of the craton; the Rokellides and Mauritanides belts run along the western side; and the Anti-Atlas belt is a typical foreland fold-thrust belt, developed by rifting, sedimentation, and volcanism along the northern margin. Such different tectonic environments can give rise to strong lateral and vertical variations in shear wave velocity structure.

3 Data and methods

For this tomographic study, we used earthquakes and seismic ambient noise data recorded at seismic stations in West Africa and the surrounding regions (Table 1 and Figure 2). We downloaded raw waveform data from the Incorporated Research Institutions for Seismology Data Management Center (IRIS-DMC) and obtained earthquake source parameters from the Global Centroid Moment Tensor catalog (Global CMT). We deconvolved instrument responses from the seismic waveforms before any further analysis.

3.1 Earthquake data processing

We analyzed vertical component broad-band or long-period seismograms from 342 earthquakes that occurred between 1996 and 2014 recorded at 12 seismic stations. We selected earthquakes with magnitudes $M \geq 5$ whose epicenters lay between -30°N, +30°N, -30°E and +30°E, added some $M \geq 4.5$ events with clear surface waves, and included some seismic events beyond these coordinates to increase azimuthal coverage. Most of the seismic events in West Africa are shallow (Suleiman et al., 1993), leading to strong fundamental mode Rayleigh waves.

Before proceeding with the dispersion analysis, we decimated all the waveforms to 0.25 s (4 Hz), then visualized them and retained those with clear dispersed surface waves. A complete list of earthquake-station

paths retained is available as an Online Resource (Table S1). Example waveforms corresponding to oceanic, ocean-continent, and continental paths are shown in Figure 3.

3.2 Ambient noise processing and cross-correlations

We downloaded vertical component data recorded between 1995 and 2015 by 34 broad-band seismic stations and performed cross-correlations between every station-pair to estimate Rayleigh wave Green's functions. Some stations recorded less than 2 years of data; others suffered interruptions of several months or years. The data availability shown in Figure 4 influenced the number of station pairs available for cross-correlation.

Imaging the subsurface structure using seismic noise tomography requires multiple analysis steps to increase the quality of the dispersion curves (Bensen et al., 2007; Lin et al., 2007; Poli et al., 2012). We processed the seismic waveforms station by station, following a procedure similar to that of Zigone et al. (2015) that aims to minimize the negative effects caused by earthquakes, temporally localized incoherent noise sources, and data irregularities. We performed a series of tests before converging on the following pre-processing scheme that maximized the cross-correlation's signal-to-noise-ratio (defined here as the maximum amplitude divided by the root-mean-square of a noise window from the correlation function's tail): decimate the signal to 1 s (1 Hz); high-pass filter at 250 s (4 mHz); clip at 15 standard deviations to remove high amplitudes and glitches; cut daily traces into 4-hour time windows; remove strong impulsive signals by discarding windows whose energy exceeds the daily average by over 30%; remove windows with gaps over 10% of the total duration; apply spectral domain whitening between 1 and 200 s period (5 and 1000 mHz frequency).

After applying this scheme on all our data, we cross-correlated the resulting waveforms across all available station pairs and stacked the correlation functions over the fullest available time period (see for example Bensen et al., 2007). When averaged over a sufficiently long period, the spatial distribution of seismic noise sources tends to homogenize, allowing us to relate the stacked correlation functions for a pair of stations to the Green's function along the path that joins them. Figure 5 shows correlation functions and their resulting stacks for two station pairs, one with 5 years and the other with 12 years of available data. The temporal stability of the correlation functions (Fig. 5a,b) indicates that most of the transient sources were properly removed from the traces by the pre-processing. The signals at positive (causal) and negative (a-causal) lags represent waves travelling in opposite directions between the two stations of a pair. The arrival times of the surface-wave packets are symmetric between the causal and a-causal parts of the stacked correlation functions (Fig. 5c,d) and increase for the more distant station pair. The amplitudes of the causal and a-causal parts are almost identical for the station-pair with 12 years of available data, indicating complete noise homogenization.

When ordered with increasing station-pair separation (Fig. 6), the stacked correlation functions filtered between 30-100 s display clear signals that arrive at positive and negative lags with arrival times consistent

with Rayleigh wave group velocities. Such simultaneity combined with only few cases of asymmetric amplitudes indicates that the overall noise field is close to being diffuse in this period range (near complete homogenization).

As in most tomography studies using seismic noise cross-correlation, we symmetrized the correlations by calculating the sum of the causal and a-causal parts for each pair of stations (Shapiro and Campillo, 2004). This process allowed us to take advantage of slight differences in frequency content in the two propagation directions.

3.3 Dispersion measurements and path selection

We computed the group-velocity dispersion curves for earthquakes and noise cross-correlations using equivalent implementations of the same approach: frequency time analysis (Dziewonski et al., 1969; Levshin et al., 1989, 1992; Ritzwoller and Levshin, 1998; Hermann, 2013), which applies a sequence of Gaussian filters at a discrete set of periods and computes the envelope of these filtered signals to create a period group-velocity diagram (see examples in Figures 7 and 8). As the frequency contents of earthquake and noise data differ, we adapted the set of Gaussian filters to each dataset: from 4 to 250 s for earthquakes and from 4 to 120 s for noise correlations.

We measured the group-velocity by picking the maximum amplitude of the envelope function at each period and estimated the uncertainty of each measurement as the width of a Gaussian approximation to the envelope function. In order to keep only reliable measurements, we selected the period range on which the maximum of the dispersion diagram corresponded to the fundamental mode Rayleigh wave, while rejecting all parts of the dispersion curves affected by scattered waves, multi-pathing effects, or overlapping overtones. We paid particular attention to the ambient noise dispersion curves, as persistant noise sources, such as the 26 s signal identified by Shapiro et al. (2006) in the Gulf of Guinea, can distort them.Figure

Figure 7 shows an example of the group-velocity dispersion analysis for the seismogram from Figure 3b, performed using the Hermann (2013) implementation of the multiple filter technique. The Rayleigh wave is well dispersed and produces a simple period group-velocity diagram with a strong, continuous ridge line along which to measure group-velocity. The maximum energy occurs between 30 and 80 s period and depends on the magnitude of the earthquake (Ms 6.0). Figure 8 shows an equivalent analysis for the symmetrized versions of the noise cross-correlation pairs presented on Figure 5, exploiting the Pedersen et al. (2003) implementation of the same multiple filter technique. The maximum energy here occurs between 20 and 40 s period and depends on the excitation spectrum of microseismic noise.

After measuring the dispersion curves, we used selection criteria specifically designed for each dataset to ensure good quality, coherent measurements.

For earthquake data, we followed the approach of Maggi et al. (2006) and Ritzwoller and Levshin (1998) and compared multiple dispersion measurements along repeatedly sampled propagation paths. This allowed

us to identify artefacts such as earthquake source errors and to avoid oversampling of certain paths that could lead to bias in the tomographic models. We formed clusters by grouping all the paths whose starting and ending points occurred within 2° of the extremities of a reference path chosen randomly from the data set; we also imposed that no path could belong to more than one cluster. We examined each cluster to identify outlier dispersion curves. After outlier rejection, we selected a representative dispersion curve from each cluster. Not all dispersion curves were part of a cluster; we analysed these single dispersion curves individually for artefacts. We retained 352 fundamental mode Rayleigh wave group-velocity dispersion curves from 147 earthquakes. Table S1 in the Online Resources lists all the corresponding paths with the period ranges retained for the inversion.

For cross-correlation data, we excluded dispersion curves computed on cross-correlation functions whose signal-to-noise ratios were smaller than 7. To ensure good sampling of the medium between the two stations, we also excluded group-velocity measurements for which the inter-station distance was smaller than 3 wavelengths. We retained 25 stations to estimate inter-station group velocity dispersion curves (Figure 4). Table S2 in Online Resources lists the station pairs with the corresponding period ranges retained for the inversion.

3.4 Regionalization of group velocity dispersion measurements

After the data processing and measurement steps described above, we obtained 4423 individual group velocity measurements between 20 and 100 s period: 3559 from the earthquake data and 864 from the noise cross-correlations.

To produce interpretable group velocity maps from these measurements, we solved the standard tomographic problem represented by the linear equation $\underline{d} = \underline{\underline{G}}\ \underline{m}$, where $d_i = x_i/U_i$ is the epicentral distance divided by the group velocity for path i, $m_j = 1/U_j$ is the group slowness in cell j of some spatial discretization of the Earth's surface, and G_{ij} is the length of path i in cell j. We assumed great-circle paths, discretized the problem using a regular latitude/longitude grid, and used the regionalization method proposed by Debayle and Sambridge (2004).

This computationally efficient method takes into account the measurement uncertainties σ_d, constrains the lateral smoothness of the inverted model using a horizontal correlation length L_{corr}, and controls the amplitude of the perturbations in the inverted model using an a-priori model variance σ_m. As with all regularization parameters, the criteria for choosing the best combination of L_{corr} and σ_m are somewhat subjective, though they remain based on common sense and make use of a-priori knowledge of the region under study. After testing different discretization grids and values of the regularization parameters, we selected a combination that produced maps consistent with the geological features of the region (sedimentary basins, mobile belt zones, shields, etc.): a $2° \times 2°$ regular grid and an a-priori model variance $\sigma_m = 0.05$ km/s. We selected the L_{corr} values for each period through a standard L-curve analysis (Hansen and

O'Leary, 1993), and chose a value near the maximum curvature of the L-curves. This analysis resulted in $L_{\text{corr}} = 300km$ for periods lower than 30s, $L_{\text{corr}} = 400km$ between 30s and 70s and $L_{\text{corr}} = 500km$ for periods longer than 70s. More information on the general effects of increasing or decreasing L_{corr} and σ_m can be found in Maggi et al. (2006), which uses the same inversion method on different data.

4 Results

Figure 9 shows the geographical distribution of dispersion measurements from our earthquake and ambient noise joint dataset at periods from 20 to 40 s. These measurements show coherent spatial structure, with slow group velocities for paths contained entirely within the continent, fast group velocities for paths contained entirely within the ocean, and intermediate velocities for paths crossing the ocean-continent boundary. The geographical distribution of measurements for periods between 70 and 100 s shows fewer systematic differences between oceanic and continental paths (Figure 11a,c,e).

After applying the Debayle and Sambridge (2004) tomographic inversion method, we obtained the group-velocity maps shown in Figures 10 and 11. The variances of these maps increase at shorter periods, indicating greater heterogeneity at shallow depths. At short periods (Figure 10a-c), we find faster group velocities in the oceanic regions (3.6 to 4 km/s) than in the continental regions (2.8 to 3.2 km/s), due to well-known differences in crustal composition and thickness. These velocities are consistent with crust over 35 km thick in the West African craton and between 9 and 12 km thick in the adjacent ocean, as found by Pasyanos et al. (2004) and Pasyanos and Nyblade (2007). The low group velocities under the Tindouf basin between 20 and 40 s period are consistent with its thick sedimentary cover. Those under the Anti-Atlas mountains at 20 and 25 s period are consistent with their recent tectonic history: their Triassic-Jurassic age normal faults reactivated following collision of Africa with Eurasia in the Cenozoic (Gomez et al., 2000). The low velocities under central Algeria between 20 and 40 s period are consistent with the 5 to 6 km thick sediments found in the region by Hadiouche and Jobert (1988).

At intermediate periods, despite less pronounced velocity contrasts, we can still distinguish the Pan-African mobile belt zones that form the eastern border of the craton (Figure 11b, also visible in Figure 10b). These zones contain several volcanic fields, have experienced tectono-thermal events within the past 650 Ma, and feature higher heat flow and possibly thinner lithosphere than the adjacent West African craton (Lesquer et al., 1989). The Taoudeni basin region shows lower group velocities up to 50 s period, consistent with the thick sedimentary layer found by Begg et al. (2009) (Figures 10 and 11b). We also find slower group velocities in the Paleoproterozoic lithosphere of the Leo Rise compared to those in the adjacent Archean lithosphere of the Man shield at 50 s period (Figure 11b). The low velocity anomalies from 50 to 70 s period in North Africa visible in Figure 11b,d are consistent with the results of Hadiouche and Jobert (1988) who found lower group-velocities extending westward from northeast Africa and attributed them to subduction between the African and European plates.

At long periods (Figure 11d,f), our model displays fast group velocities under the Man-Leo and the Reguibat shields, indicating cold, thick lithospheric roots, and lower group velocities under the mobile belt zone, indicating thinner lithosphere also seen by Priestley et al. (2008). The high velocity root beneath the West African craton extends northward up to the Anti-Atlas in the Priestley et al. (2008) model, while in our model it stops at the southern edge of the Tindouf basin.

The roots under the Requibat and Man-Leo shields seem to be separated by a region of lower group velocity that could correspond to the Guinean-Nubian lineament, a major fracture system that extends from the coast of Senegal to the Red Sea (Wilson and Guiraud, 1992; Guiraud et al., 2005). However, the lower group velocities could also be an artefact caused by the thick sediments in the Taoudeni basin (Begg et al., 2009). In order to distinguish between these two interpretations, we would need to consider seismic observables with different vertical sensitivities, for example Rayleigh wave phase velocities, or Love wave phase or group velocities.

5 Discussion

We produced images of the seismic lithospheric structures of West Africa using group-velocity dispersion curves from both noise correlations and earthquakes. By combining these two sources, we increased the density of surface-wave measurements within this undersampled area and improved the resolution of our seismic models. The resulting Rayleigh-wave group-velocity maps correlate well with major tectonic features in the region. At short periods (Figure 10), our group-velocities highlight differences in crustal thickness: they are fast in the oceans and and slow on the continents. The Tindouf basin and the Anti-Atlas are the slowest continental regions, indicating recent tectonic activity and/or thick sediments. We also observe slow group-velocities under the Taoudeni basin which likely reflects thick sediments (Begg et al., 2009). At an even finer scale, we believe we can see differences between the Paleoproterozoic basement (Leo Rise) and the Archean basement (Man shield), not mentioned in previous studies. At long periods (Figure 11), the fast velocities at the roots of the Man-Leo and the Reguibat shields indicate cold, thick lithosphere under the craton. Our high group velocity anomalies at 100s of period are consistant with estimated lithospheric thickness computed by Pasyanos et al. (2014) and Priestley and Tilmann (2009). Our results are also compatible with the global tomographic model obtained by Ma et al. (2014), which shows high phase-velocity over the West African Croton at low-frequency. Our images show lower group-velocities under the Pan-African mobile belt zones, probably due to thinner lithosphere.

When creating tomographic images using ambient noise and earthquakes, we need to ensure that the empirical Green's functions we obtain from the noise cross-correlations are accurate enough for us to obtain dispersion measurements compatible with those obtained from earthquakes. We tested this in our own dataset by comparing waveforms and dispersion curves from both source types that sample the same region. Figure 12 shows such a comparison for the path between ASCN and TSUM, also sampled by an earthquake

located near ASCN. The surface-waves resemble each other greatly, confirming that the cross-correlations do indeed provide an accurate approximation to the Rayleigh wave Green's function between the pair of stations (Figure 12b). The two dispersion diagrams also resemble each other between 10 and 50s (Figure 12c,d). At longer periods, there seems to be more energy in the cross-correlation than was generated by the moderate magnitude earthquake. Such comparisons convinced us that our earthquake and noise-based surface waves contained similar structural information, and that we could indeed measure and invert them together.

Ambient noise and earthquakes provide measurements in complementary period bands. Strong interactions between ocean waves and the solid Earth generate most of the microseimic noise recorded by seismological stations and produce stable ambient noise correlation functions in the 1-30s period band (Longuet-Higgings, 1950; Hasselmann, 1963; Campillo and Roux, 2015). At longer periods, the energy of the available noise decreases, which means we need to stack over longer time periods to obtain stable cross-correlation functions (Shapiro and Campillo, 2004; Bensen et al., 2007). Figure 13a shows the number of measurements (paths) as a function of period for both ambient noise and earthquakes. For ambient noise, this number remains constant from 20 s to 40s then decreases rapidly after 50 seconds because we lack noise sources at longer periods. For earthquakes, the number of measurements increases progressively from 20 s to 40s to reach a maximum between 40s to 70s, because the energy provided by earthquakes increases in this period range. Although we obtained surface wave dispersions up to 200s for some large seismic events, these were too few to produce meaningful dispersion maps for periods above 150s, confirming what we have known for two decades now: the reliability of earthquake based Rayleigh-wave group-velocity maps across large continental regions degrades sharply at periods below 20 s and above 150-200s (Ritzwoller and Levshin, 1998).

Our joint dataset provides good spatial coverage from 20 to 100 s period. We obtained many more group-velocity measurements from earthquakes than from seismic noise, however the latter make up one-quarter to one-third of all measurements made below 35s period (see Figure 13a). Noise measurements are the only ones that provide coverage of the eastern part of the region; they also contribute key paths that improve the azimuthal coverage of the more densely sampled regions (see Figure 13b for a comparison of earthquake and noise-based paths at 20 s period). By combining noise and earthquake data, we increased the number of measurements at each period and improved their spatial coverage, both of which are necessary to reduce smearing and bias in group-velocity maps and improve their resolution.

The quality of tomography models is controlled by the quantity and quality of the measurements, by the path distribution (density of paths, azimuthal coverage, average path length), and by the weighting and damping applied during inversion (e.g. Vdovin et al., 1999). We used standard checkerboard resolution tests with the same path distribution, measurement uncertainties, correlation length and a-priori model variance

as the real data to investigate the stability and lateral resolution of our group-velocity maps. We created synthetic datasets using checkerboard patterns of different sizes around a mean velocity of 3.7 km/s.

Figure 14 shows the synthetic pattern for a $10^\circ \times 10^\circ$ checkerboard test and the results of three inversions using path distributions and measurement uncertainties observed at 20 s period (note that this is not the period at which we have the densest coverage). Using only earthquake measurements (Figure 14b), we recovered the correct positions of the velocity anomalies in the center and west of the study area. The excessive amplitudes of both positive and negative anomalies in the central region indicate bias caused by paths radiating outwards with almost no crossing paths. Poor azimuthal coverage also caused smearing on the northern and eastern edges of the region. Using only noise measurements (Figure 14c), we recovered more velocity anomalies on the northern and eastern edges, with less bias and smearing thanks to a more balanced azimuthal distribution. By combining the two types of data (Figure 14d), we improved the resolution for the entire study area and reduced the bias in the central region. Eastern Niger and the subduction zone between North Africa and Europe remained poorly resolved due to low path coverage in these areas.

Figure 15 shows results of checkerboard tests using the path distribution and measurement uncertainties of the combined dataset at 20 s period and checkerboard sizes of $9^\circ \times 9^\circ$ and $6^\circ \times 6^\circ$. We recovered correct velocity anomalies over most of the study area for the $9^\circ \times 9^\circ$ test (Figure 15b), and over the southern part of West Africa for the $6^\circ \times 6^\circ$ test (Figure 15d). We therefore conclude that our combined dataset allows us to achieve an approximate resolution of 6 degre in the southern part of West-Africa and 9 degre over the rest of the region, with poorer resolution and smearing confined to Eastern Niger and North Africa.

Comparing the resolution of different tomographic images can be delicate, as few authors publish comparable tests. Of the handful of surface-wave tomography studies that cover West Africa, Pasyanos et al. (2001) could not recover $8^\circ \times 8^\circ$ checkerboard anomalies in central and West Africa, and Priestley et al. (2008) recovered $10^\circ \times 10^\circ$ checkerboard anomalies in the same region but showed no results from smaller ones. The resolution of these studies corresponds to the one we obtained using only earthquake data (Figure 14b). We can therefore be confident that adding noise-derived group-velocity measurements to our dataset led to better resolution of West African structures than previous studies.

We purposely restricted this study to generating group-velocity maps, without attempting to invert either our original group-velocity dispersion measurements or our group-velocity maps to obtain path-wise or point-wise profiles of V_S as a function of depth. Group-velocity depth inversions are notoriously non-linear and unstable, and need to be combined with other information (e.g., group and phase velocities of both Rayleigh and Love waves, fundamental and higher modes) to produde $V_S(z)$ profiles usable for structural interpretation. As compiling that additional information may prove difficult with the data available in West Africa, we prefer an alternate strategy. We plan a two-pronged approach: first obtain unbiased group-velocity dispersion maps with full resolution and uncertainty information using the recently developed SOLA Backus-Gilbert inverse methods of Zaroli (2016) and Zaroli et al. (2017), then move away from

dispersion measurements altogether and perform full-waveform inversion of our data-set using 3D surface-wave sensitivity kernels and the SOLA Backus-Gilbert approach to obtain a 3D V_S model.

6 Conclusion

We produced Rayleigh-wave group-velocity maps of west Africa from 20 to 100 s, using data from regional earthquakes and seismic ambient noise cross-correlation. By combining them, we increased the density and azimuthal coverage of our group-velocity measurements and improved the spatial resolution of our group-velocity maps.

At short periods, our Rayleigh-wave group-velocity maps highlight differences in crustal thickness (ocean and continent), recent tectonic activity (e.g. Anti-Atlas), and thick sediments (e.g. Tindouf and Taoudeni basins). At long periods, we found lower velocities due to hot, thin lithosphere under the Pan-African mobile belt and faster velocities due to cold, thick lithosphere under the Man-Leo and Reguibat shields.

West Africa can teach us much about the early tectonic history of Earth, if we are willing to listen. Our higher resolution group-velocity maps advance us a step towards answering questions regarding the detailed lithospheric structure and tectonic processes of West Africa; they will also help us generate improved models for locating and discriminating small local or regional seismic events. Achieving these goals in full will require adopting new inversion strategies that yield unbiased maps with full resolution and uncertainty information (e.g. SOLA Backus-Gilbert inversions), performing more complete measurements (e.g. surface waveform measurements with their corresponding finite-frequency sensitivity kernels), and, most importantly, acquiring more data by deploying seismic stations in strategic locations.

Acknowledgements The research described herein used seismological data from various global networks available through the Incorporated Research Institutions for Seismology (IRIS) Data Management Center (including Africa Array (AF), GEOSCOPE (G), Global Seismograph Network (GSN-IRIS/USGS), Global Telemetered Seismograph Network (GTSN-USAF/USGS), Instituto Superior Tecnico Broadband Seismic Network (IP), IRIS PASSCAL Experiment Stations (XB), MEDNET Project (MN), Morocco-Muenster (3D), and Seismic Network of Tunisia (TT)). We are grateful to the operators of these networks for ensuring the high quality of the data and making them publicly available. Earthquake parameters were obtained from the Global CMT catalog.

Y. Ouattara was supported by the Comprehensive Nuclear-Test-Ban Treaty Organization (CTBTO) Young Scientist Award Grant, the Lamto Geophysical Station (Ivory Cost), and the CNRS-INSU TelluS-SYSTER program. Additional support in the form of computer equipment was provided by Institut de Physique du Globe de Strasbourg (IPGS). Y. Ouattara would like to thank Professor A. Diawara, director of the Lamto Geophysical Station, for his advice and moral support in seeking a PhD in seismology in France, and Professor B. C. Sombo for accepting him in his research laboratory in Abidjan and for supervising part of his thesis work. The manuscript benefitted from constructive comments by Michael Pasyanos and Editor Mariano Garcia-Fernandez.

References

Becker TW (2012) On recent seismic tomography for the western United States. Geochem Geophys Geosyst 13, doi:10.1029/2011GC003977

Begg GC, Griffin WL, Natapov LM, O'Reilly SY, Grand SP, O'Neill CJ, Hronsky JMA, Djomani YP, Swain CJ, Deen T, Bowden P (2009) The lithospheric architecture of Africa: Seismic tomography, mantle petrology, and tectonic evolution. Geosphere 5:23–50, doi: 10.1130/GES00179.1

Ben-Zion Y (2008) Collective behavior of earthquakes and faults: Continuum-discrete transitions, progressive evolutionary changes, and different dynamic regimes. Reviews of Geophysics 46, doi:0.1029/2008RG000260

Bensen GD, Ritzwoller MH, Barmin MP, Levshin AL, Lin F, Moschetti MP, Shapiro NM, Yang Y (2007) Processing seismic ambient noise data to obtain reliable broad-band surface wave dispersion measurements. Geophys J Int 169:1239–1260, doi: 10.1111/j.1365-246X.2007.03374.x

Bills BG, Adams KD, Wesnousky SG (2007) Cosity structure of the crust and upper mantle in western Nevada from isostatic rebound patterns of the late Pleistocene Lake Lahontan high shoreline. J Geophys Res 112, doi:10.1029/2005JB003941

Binks RM, Fairhead JD (1992) A plate tectonic setting for Mesozoic rifts of West and Central Africa. Tectonophysics 213:141–151

Bird P (2003) An updated digital model of plate boundaries. Geochem Geophys Geosyst 4, doi:10.1029/2001GC000252

Campillo M, Roux P (2015) Crust and Lithospheric Structure - Seismic Imaging and Monitoring with Ambient Noise Correlations. In: Treatise on Geophysics, Elsevier, pp 391–417

Chanard K, Avouac J, Ramillien G, Genrich J (2014) Modeling deformation induced by seasonal variations of continental water in the Himalaya region: Sensitivity to Earth elastic structure. Journal of Geophysical Research: Solid Earth 119:5097–5113

Craig TJ, Chanard K, Calais E (2017) Hydrologically-driven crustal stresses and seismicity in the New Madrid Seismic Zone. Nature Communications 8:2143, doi:10.1038/s41467-017-01696-w

Debayle E, Sambridge M (2004) Inversion of massive surface wave data sets: Model construction and resolution assessment. J Geophys Res 109, doi:10.1029/2003JB002652

Djomani YHP (1993) Apport de la gravimétrie à l étude de la lithosphère continentale et implications géodynamiques : Etude d'un bombement intraplaque : Le massif de l'Adamaoua (Cameroun). Thèse de Doctorat, Université PARIS Xl ORSAY, Spécialité : Géophysique p 229

Dorbath L, Montagner JP (1983) Upper mantle heterogeneities in Africa deduced from Rayleigh wave dispersion. Physics of the Earth and Planetary Interieur 32:218–225

Dziewonski A, Bloch S, Landisman M (1969) A technique for the analysis of transient seismic signals. Bull seis Soc Am 59:427–444

Fairhead JD, Reeves CV (1977) Teleseismic delay times, bouguer anomalies and inferred thickness of the african lithosphere. Earth and Planetary Science Letters 36:63–76

Gangopadhyay A, Pulliam J, Sen MK (2007) Waveform modelling of teleseismic S, Sp, SsPmP, and shear-coupled PL waves for crust- and upper-mantle velocity structure beneath Africa. Geophys J Int 170:1210–1226, doi: 10.1111/j.1365-246X.2007.03470.x

Gomez F, Beauchamp W, Barazangi M (2000) Role of the Atlas Mountains (Northwest Africa) within the African-Eurasian Plate-Boundary Zone. Geology 28(9):775–778, doi: doi.org/10.1130/0091-7613

Guiraud R, Bosworth W, Thierry J, Delplanque A (2005) Phanerozoic geological evolution of Northern and Central Africa: An overview. Journal of African Earth Sciences 43:83–143

Hadiouche O, Jobert N (1988) Geographical distribution of surface-wave velocities and 3-D upper-mantle structure in Africa. Geophysical Journal 95:87–109

Hadiouche O, Jobert N, Montagner JP (1989) Anisotropy of the African continent inferred from surface waves. Phys Earth Planet Inter 58:61–89

Hansen PC, O'Leary DP (1993) The use of the L-curve in the regularization of discrete ill-posed problems. SIAM J Sci Comp 14(6):1487–1503

Hasselmann K (1963) A Statistical Analysis of the Generation of Microseisms. Reviews of Geophysics and Space Physics 1:177–210

Hazler SE, Sheean AF, McNamara DE, Walter WR (2001) One-dimensional Shear Velocity Structure of Northern Africa from Rayleigh Wave Group Velocity Dispersion. Pure appl Geophys 158:1475–1493

Hermann RB (2013) Computer programs in seismology: An evolving tool for instruction and research. Seismological Research Letters 84:1081–1088, doi:10.1785/0220110096

Lesquer A, Bourmatte A, Ly S, Dautria J (1989) First heat flow determination from the central Sahara :relationship with the Pan-African belt and Hoggar domal uplift. Journal of African Earth Sciences 9:41–48

Levshin A, Ratnikova L, Berger J (1992) Peculiarities of surface wave propagation across central Eurasia. Bull seism Soc Am 82:2464–2493

Levshin AL, Yanovskaya TB, Lander AV, Bukchin BG, Barmin MP, Ratnikova LI, Its EN (1989) Seismic Surface Waves in a Laterally Inhomogeneous Earth. Kluwer, Dordrecht

Lin FC, Ritzwoller MH, Townend J, Bannister S, Savage MK (2007) Ambient noise Rayleigh wave tomography of New Zealand. Geophys J Int 170:649–666, doi: 10.1111/j.1365-246X.2007.03414.x

Longuet-Higgings M (1950) A theory of the origin of microseisms. Philosophical Transactions of the Royal Society of London A243(857):1–35

421 Ma Z, Masters G, Laske G, Pasyanos M (2014) A comprehensive dispersion model of surface wave phase
422 and group velocity for the globe. Geophys J Int 199:113–135, doi: 10.1093/gji/ggu246
423 Maggi A, Debayle E, Priestley K, Barruol G (2006) Multimode surface waveform tomography of the
424 Pacific Ocean: a closer look at the lithospheric cooling signature. Geophys J Int 166:1384–1397, doi:
425 10.1111/j.1365-246X.2006.03037.x
426 Pasyanos ME, Nyblade AA (2007) A top to bottom lithospheric study of Africa and Arabia. Tectonophysics
427 444:27–44, doi:10.1016/j.tecto.2007.07.008
428 Pasyanos ME, Walter WR, Hazler SE (2001) A Surface Wave Dispersion Study of the Middle East and
429 North Africa for Monitoring the Comprehensive Nuclear-Test-Ban Treaty. Pure and Applied Geophysics
430 158:1445–1474
431 Pasyanos ME, Walter WR, Flanagan MP, Goldstein P, Bhattacharyya J (2004) Building and Testing an a
432 priori Geophysical Model for Western Eurasia and North Africa. Pure Appl Geophys 161:235–181, doi:
433 10.1007/s00024-003-2438-5
434 Pasyanos ME, Masters TG, Laske G, Ma Z (2014) LITHO1.0: An updated crust and lithospheric model of
435 the Earth. Earth, J Geophys Res Solid Earth 119:2153–2173, doi:10.1002/2013JB010626
436 Pedersen HA, Mars J, Amblard PO (2003) Improving group velocity measurements by energy reassignment.
437 Geophysics 68:677–684
438 Poli P, Pedersen HA, Campillo M, the POLENET/LAPNET Working Group (2012) Noise directivity and
439 group velocity tomography in a region with small velocity contrasts: the northern Baltic Shield. Geophys
440 J Int 192:413–424, doi: 10.1093/gji/ggs034
441 Priestley K, Tilmann F (2009) Relationship between the upper mantle high velocity seismic lid and the
442 continental lithosphere. Lithos 109, doi:10.1016/j.lithos.2008.10
443 Priestley K, McKenzie D, Debayle E, Pilidou S (2008) The African upper mantle and its relationship to
444 tectonics and surface geology. Geophys J Int 175:1108–1126, doi: 10.1111/j.1365-246X.2008.03951.x
445 Ritsema J, van Heijst H (2000) New seismic model of the upper mantle beneath Africa. Geology 28:63–66
446 Ritzwoller MH, Levshin AL (1998) Eurasian surface wave tomography : Group velocities. Journal of Geo-
447 physical Research 103:4839–4878
448 Ritzwoller MH, Shapiro NM, Levshin AL, Leahy GM (2001) Crustal and upper mantle structure beneath
449 Antarctica and surrounding oceans. Journal of Geophysical Research 106:30645–30670
450 Romanowicz B (2003) Global Mantle Tomography: Progress Status in the Past 10 Years. Annual Review
451 of Earth and Planetary Sciences 31:303–328, doi:10.1146/annurev.earth.31.091602.113555
452 Sebai A, Stutzmann E, Montagner JP, Sicilia D, Beucler E (2006) Anisotropic structure of the African
453 upper mantle from Rayleigh and Love wave tomography. Physics of the Earth and Planetary Interiors
454 155:48–62, doi:10.1016/j.pepi.2005.09.009

Shapiro NM, Campillo M (2004) Emergence of broadband Rayleigh waves from correlations of the ambient seismic noise. Geophys Res Lett 31, doi:10.1029/2004GL019491

Shapiro NM, Campillo M, Stehly L, Ritzwoller MH (2005) High-Resolution Surface-Wave Tomography from Ambient Seismic Noise. Science 307:1615–1618

Shapiro NM, Ritzwoller MH, Bensen GD (2006) Source location of the 26 sec microseism from cross-correlations of ambient seismic noise. Geophys Res Lett 33, doi:10.1029/2006GL027010

Shen W, Ritzwoller MH (2016) Crustal and uppermost mantle structure beneath the United States. J Geophys Res Solid Earth 121:4306–4342, doi:10.1002/2016JB012887

Shen W, Ritzwoller MH, Schulte-Pelkum V (2013) A 3-D model of the crust and uppermost mantle beneath the Central and Western US by joint inversion of receiver functions and surface wave dispersion. Journal of Geophysical Research: Solid Earth 118:262–176, doi:10.1029/2012JB009602

Suleiman AS, Doser DI, Yarwood DR (1993) Source parameters of earthquakes along the coastal margin of West Africa and comparisons with earthquakes in other coastal margin settings. Tectonophysics 222:79–91

Vdovin O, Rial JA, Levshin AL, Ritzwoller MH (1999) Group-velocity tomography of South America and the surrounding oceans. Geophys J Int 136:324–340

Villasenor A, Ritzwoller M, Levshin A, Barmin M, Engdahl E, Spakman W, Trampert J (2001) Shear velocity structure of central Eurasia from inversion of surface wave velocities. Physics of the Earth and Planetary Interiors 123:169–184

Wilson M, Guiraud R (1992) Magmatism and rifting in Western and Central Africa, from Late Jurassic to Recent times. Tectonophysics 213:203–225

Yang Y, Li A, Ritzwoller MH (2008a) Crustal and uppermost mantle structure in southern Africa revealed from ambient noise and teleseismic tomography. Geophys J Int 174:235–248, doi: 10.1111/j.1365-246X.2008.03779.x

Yang Y, Ritzwoller MH, Lin FC, Moschetti MP, Shapiro NM (2008b) Structure of the crust and uppermost mantle beneath the western United States revealed by ambient noise and earthquake tomography. J Geophys Res 113, doi:10.1029/2008JB005833

Yao H, Beghein C, van der Hilst RD (2008) Surface wave array tomography in SE Tibet from ambient seismic noise and two-station analysis – II. Crustal and upper-mantle structure. Geophys J Int 173:205–219, doi:10.1111/j.1365-246X.2007.03696.x

Yao H, van der Hilst RD, Montagner J (2010) Heterogeneity and anisotropy of the lithosphere of SE Tibet from surface wave array tomography. J Geophys Res 115, doi:10.1029/2009JB007142

Zaroli C (2016) Global seismic tomography using Backus-Gilbert inversion. Geophysical Journal International 207, doi:10.1093/gji/ggw315

Zaroli C, Koelemeijer P, Lambotte S (2017) Toward Seeing the Earth's Interior Through Unbiased Tomographic Lenses. Geophysical Research Letters 44, doi:10.1002/2017GL074996

490 Zigone D, Ben-Zion Y, Campillo M, Roux P (2015) Seismic Tomography of the Southern California Plate
491 Boundary Region from Noise-Based Rayleigh and Love Waves. Pure and Applied Geophysics 172:1007–
492 1032, doi:10.1007/s00024-014-0872-1

Table 1 Seismic stations used in this study. Stations indicated by * were used for dispersion measurements for both earthquake and seismic noise data; stations indicated by ** were used only for earthquakes; the others were used only for ambient noise cross-correlation. Network initials are as follows: Africa Array (AF), GEOSCOPE (G), Global Seismograph Network (GSN-IRIS/USGS), Global Telemetered Seismograph Network (GTSN-USAF/USGS), Instituto Superior Tecnico Broadband Seismic Network (IP), IRIS PASSCAL Experiment Stations (XB), MEDNET Project (MN), Morocco-Muenster (3D), and Seismic Network of Tunisia (TT).

Station	Network	Latitude($^\circ N$)	Longitude($^\circ E$)	Instrument	Location ID
ASCN*	II	-7.9327	-14.3601	Trillium 120 BB	10
BGCA	GT	5.1763	18.4242	KS-54000	
CM01	XB	2.3890	9.8340	Guralp CMG3T	02
CM10	XB	4.2230	10.6190	Guralp CMG3T	02
CM20	XB	6.2250	10.0540	Guralp CMG3T	02
CM30	XB	9.7570	13.9500	Guralp CMG3T	02
CMLA**	II	37.7637	-25.5243	Streckeisen STS-2	10
DBIC*	GT	6.6701	-4.8565	KS-54000	00
IFE	AF	7.5466	4.4569	EP-105	
KOWA*	IU	14.4967	-4.0140	Trillium 240 BB	10
MACI	IU	28.2502	-16.5081	Streckeisen STS-1V/VBB	
MBO*	G	14.3920	-16.9554	Streckeisen STS-1	10
MM07	3D	30.2584	-5.6084	Trillium 120 s	
MM13	3D	30.5392	-9.5835	Trillium 120 s	
MSKU*	IU	-1.6557	13.6116	Streckeisen STS-1V/BB	00
MTOR	IP	28.4948	-9.8487	Streckeisen STS-2/120 s	
PM01	XB	35.7016	-5.6543	Guralp CMG3T	
RTC	MN	33.9881	-6.8569	Streckeisen STS-1V/VBB	
SACV*	II	14.9702	-23.6085	Trillium 120 BB	10
SEHL*	II	-15.9588	-5.7457	Streckeisen STS-2	10
SVMA	AF	16.8440	-24.9250	Guralp CMG-3ESP/100s	
TAM*	G	22.7914	5.5283	Streckeisen STS-1	00
TATN*	TT	32.5787	10.5292	Streckeisen STS-2/120 s	00
THTN*	TT	35.5616	8.6881	Streckeisen STS-2/G3	00
TSUM*	IU	-19.2022	17.5838	Streckeisen STS-1H/VBB	
WDD	MN	35.8373	14.5242	Streckeisen STS-2	

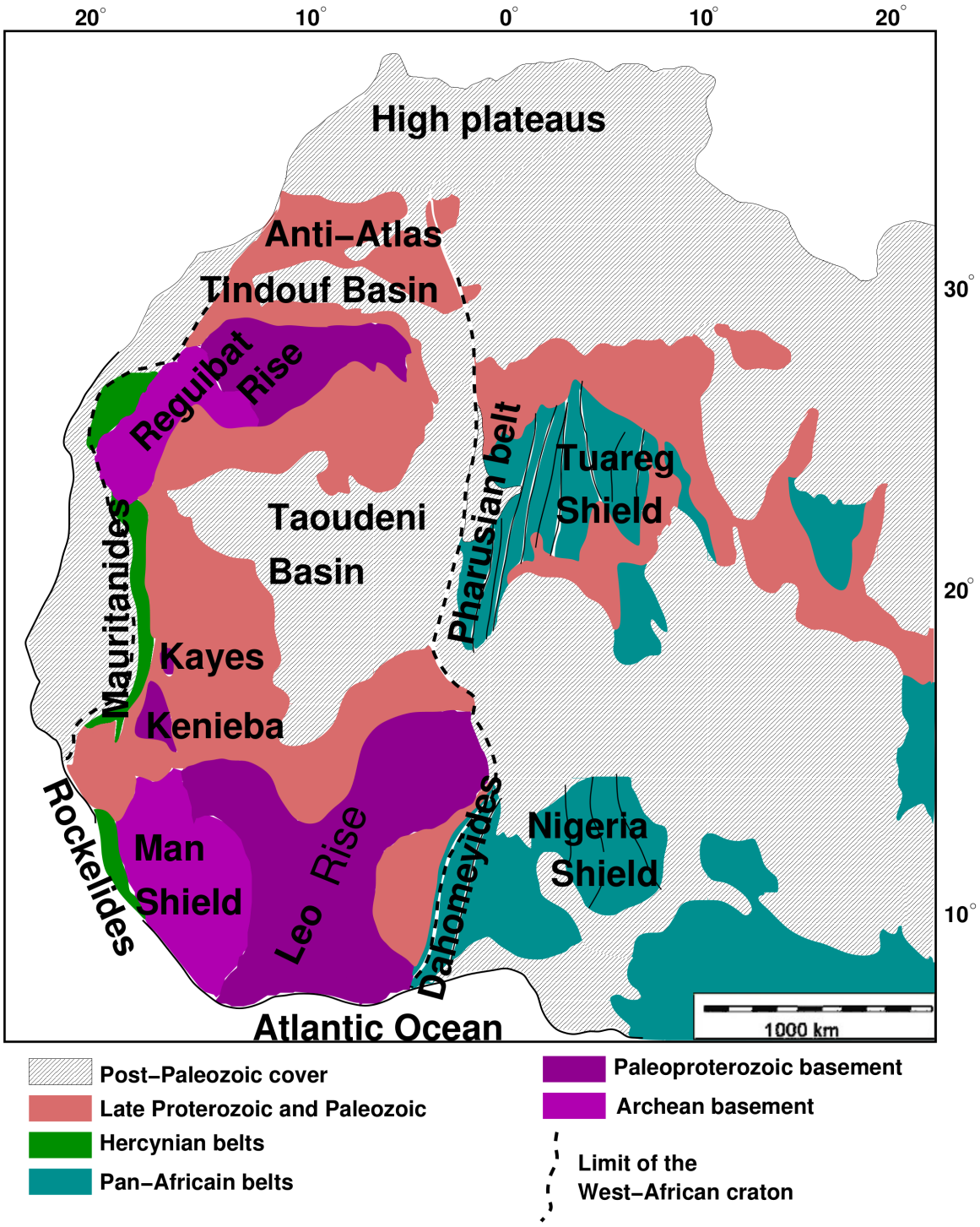

Fig. 1 Simplified geological map of West Africa, indicating the major geological features discussed in this paper.

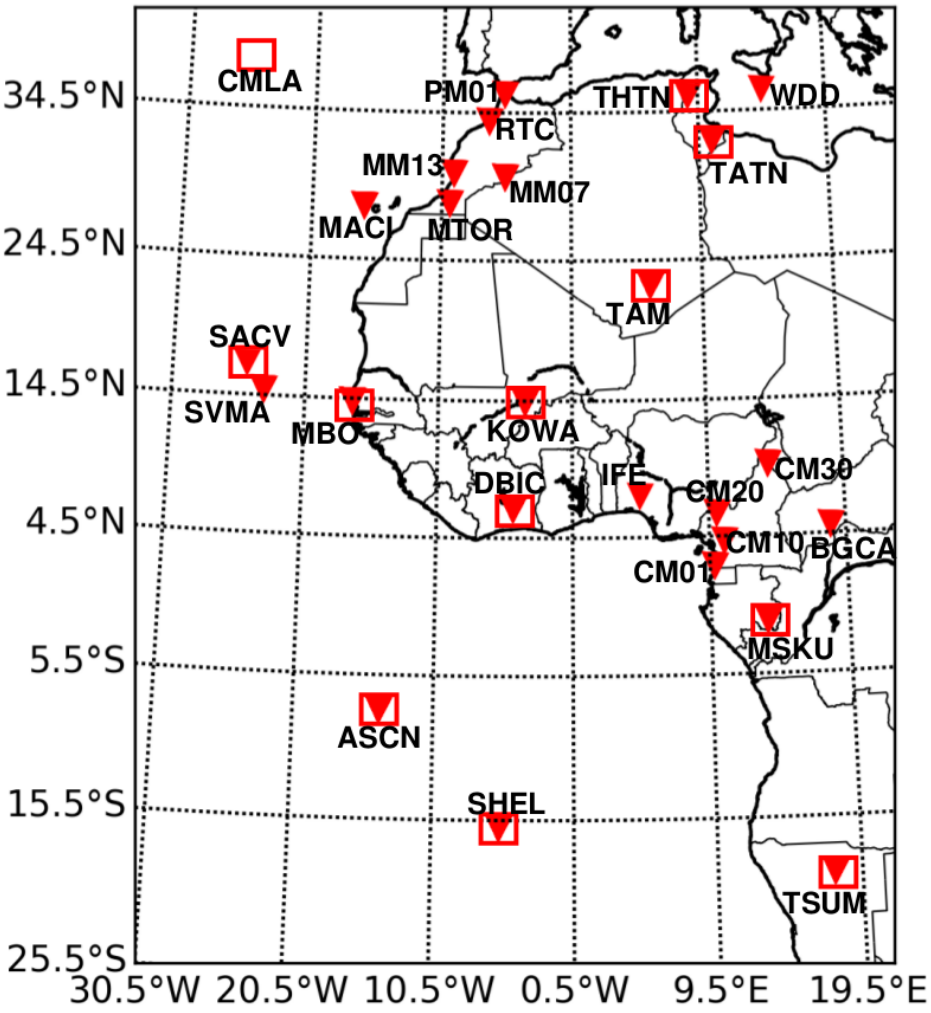

Fig. 2 Locations of stations used in this study. Squares indicate stations used for dispersion measurements using earthquake data; triangles indicate stations used for cross-correlation analysis.

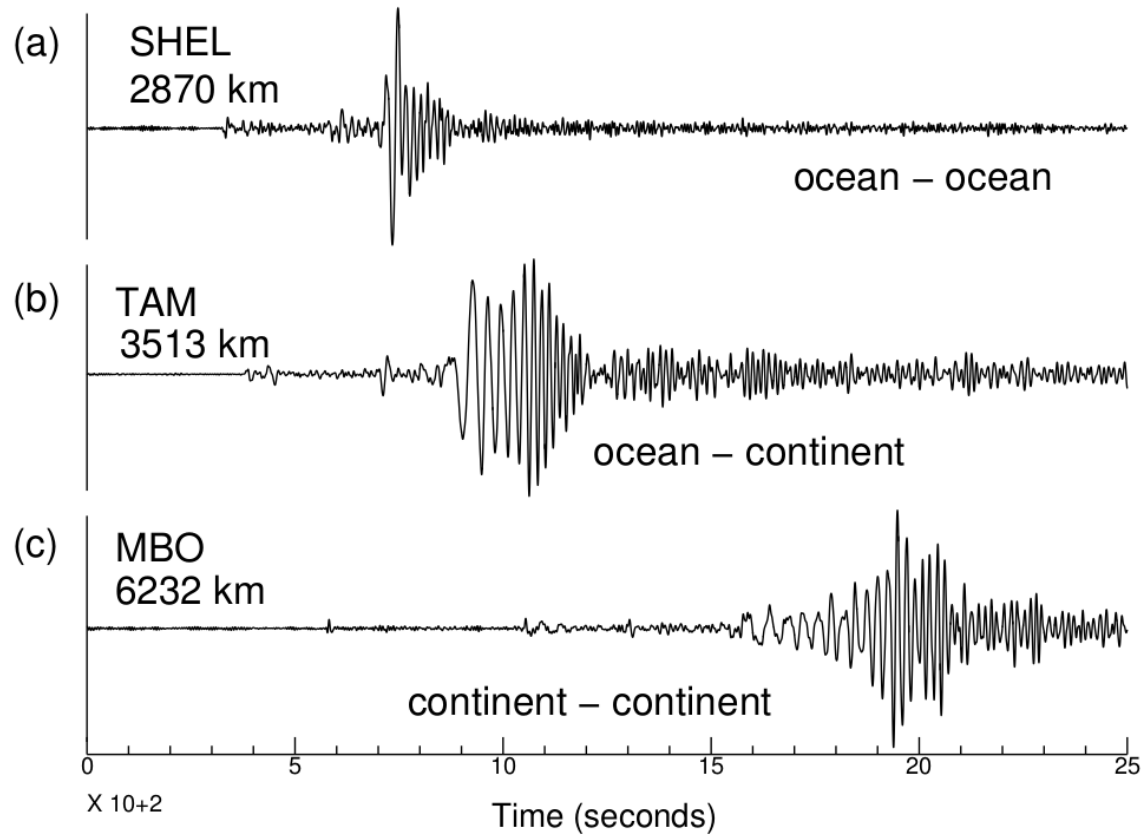

Fig. 3 Examples of vertical-component velocity seismograms used for dispersion measurements, filtered between 20 s and 100s. Station responses have been removed and amplitudes have been scaled. Station names and epicentral distances are shown. Events parameters from the Global CMT catalog: (a) 15/05/2011, Ms 6.1, depth 12.78 km (0.87°N, 25.62°W); (b) 29/11/2011, Ms 6.0, depth 12 km (1.28°S, 15.60°W); (c) 19/12/2009, Ms 6.0, depth 12 km (10.02°S, 33.93°E).

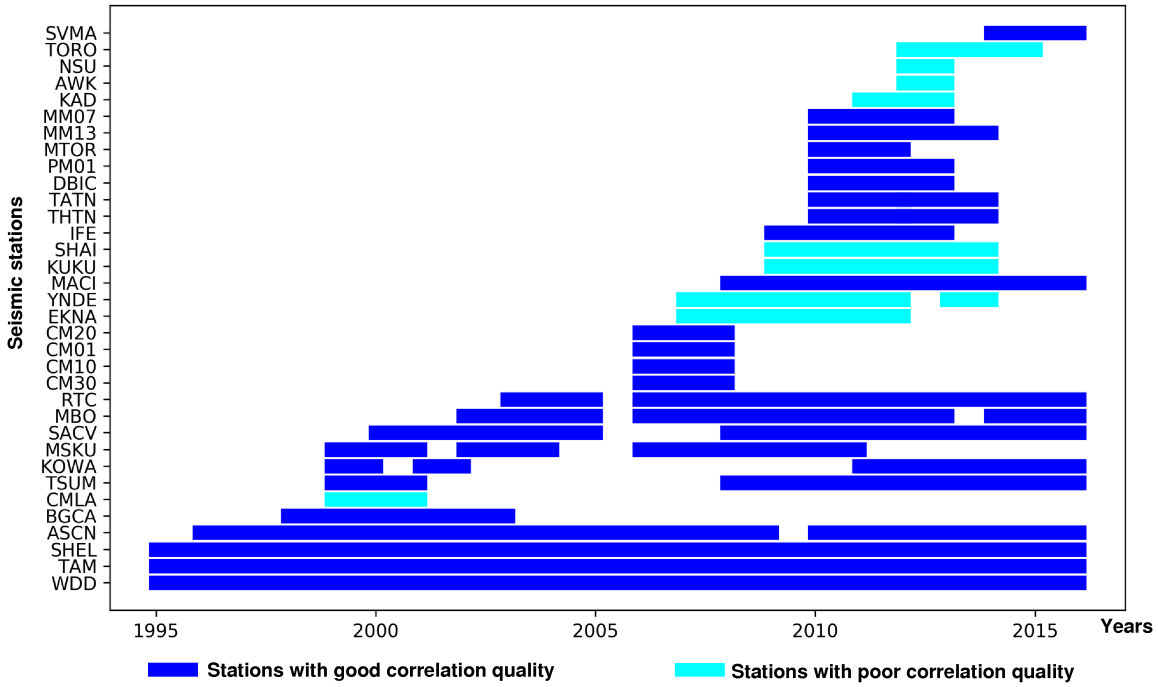

Fig. 4 Data availability for all stations used for cross-correlation analysis. Good quality stations (in dark blue) yielded cross-correlation functions with signal-to-noise ratios greater than 7. These were used to create group-velocity maps.

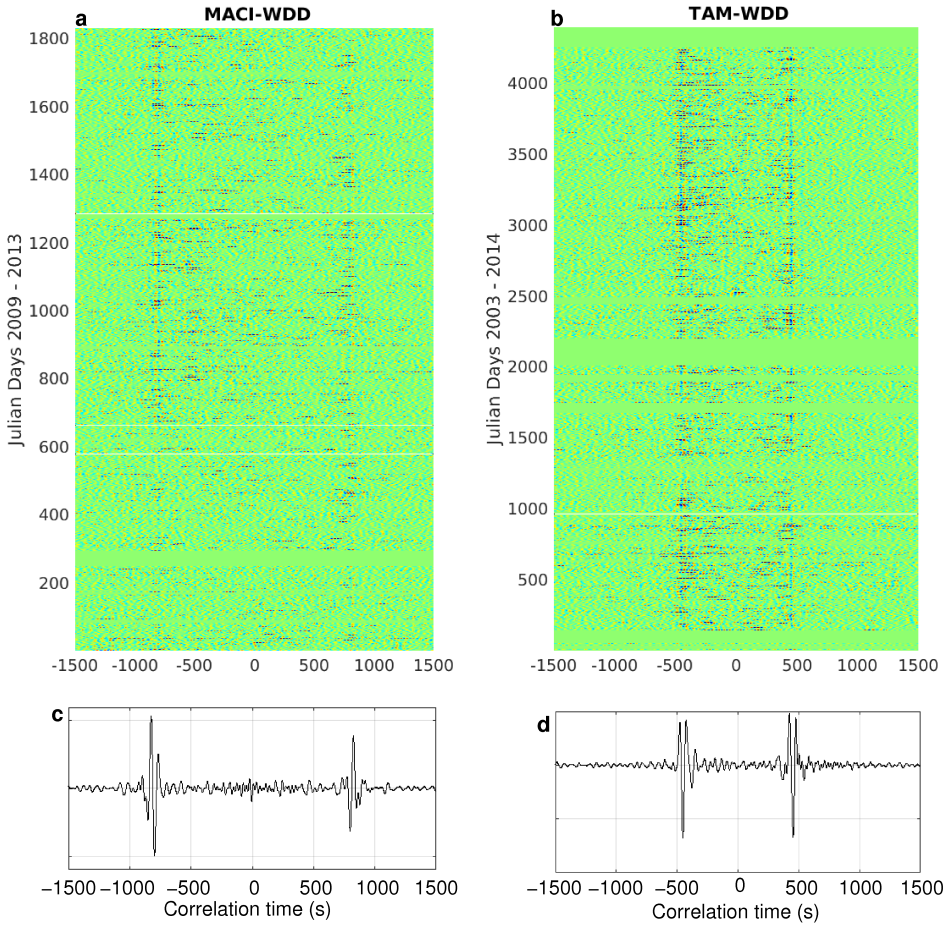

Fig. 5 Cross-correlograms (a, b) and stacks (c, d) filtered between 30 and 100 s for two station pairs. Panels (a) and (c) correspond to the station-pair MACI - WDD (3034 km distance) stacked from 2009 to 2013; pannels (b) and (d) correspond to station pair TAM - WDD (1687 km distance) stacked from 2003 to 2014.

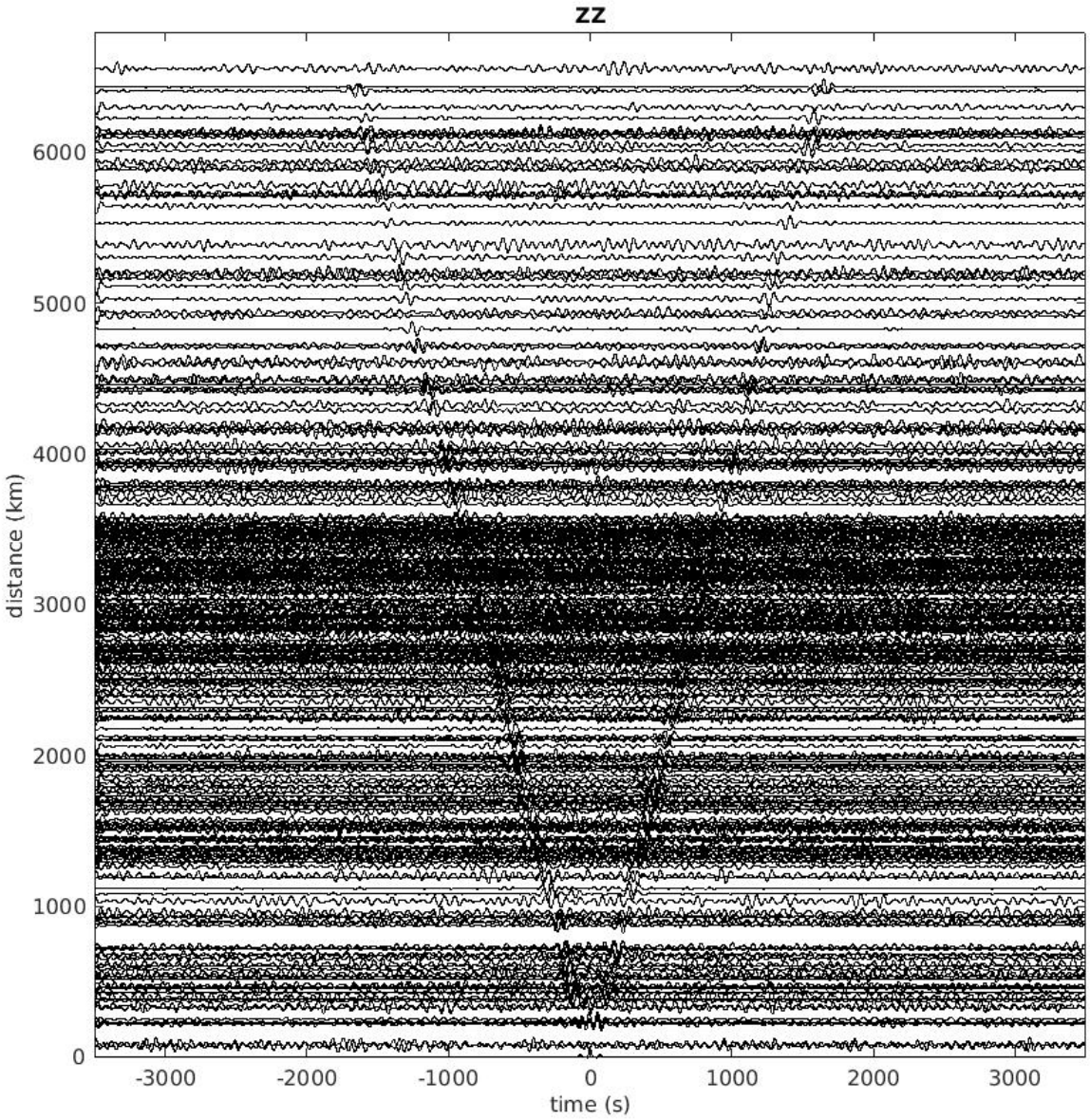

Fig. 6 Stacked vertical component cross-correlation functions filtered around 30 and 100 s and ordered with increasing station distance.

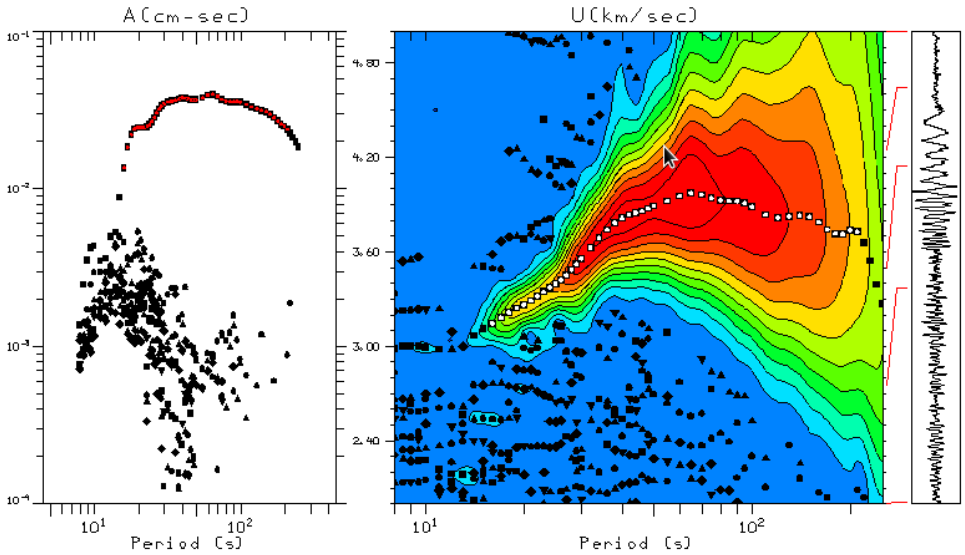

Fig. 7 Example of group velocity measurements using the Hermann (2013) implementation of the multiple filter technique on the seismogram from Figure 3b: The left panel shows the spectral amplitude as a function of period, the center panel shows the contours of the period group-velocity diagram that were used to make the dispersion measurement, and the right panel shows the waveform itself. The colors on the period group-velocity diagram indicate relative energy. The measured dispersion curve is indicated by red dots on the spectral amplitude plot and white dots on the period group-velocity diagram.

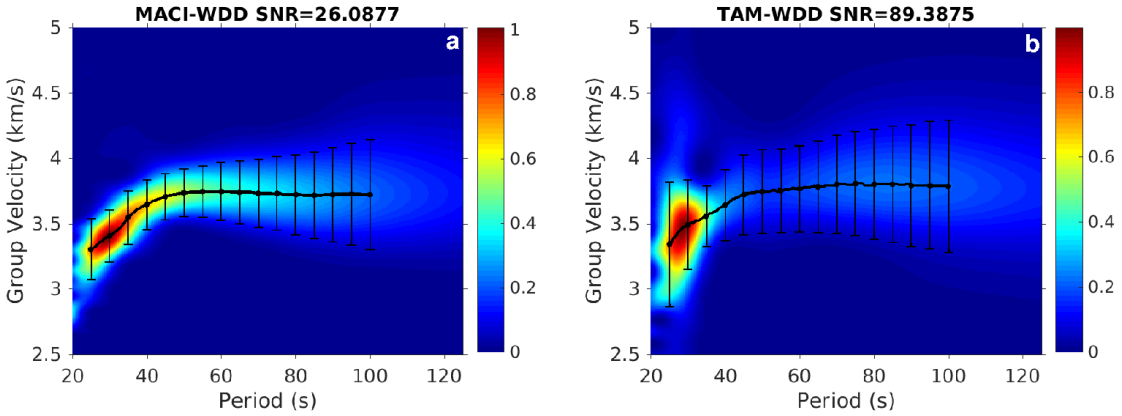

Fig. 8 Group velocity dispersion diagrams for symmetric component. The thick black curves indicate the measured Rayleigh wave dispersion curves; the error-bars indicate 1-σ uncertainties; the color scale indicates relative energy. The maximum energy is observed at short period.

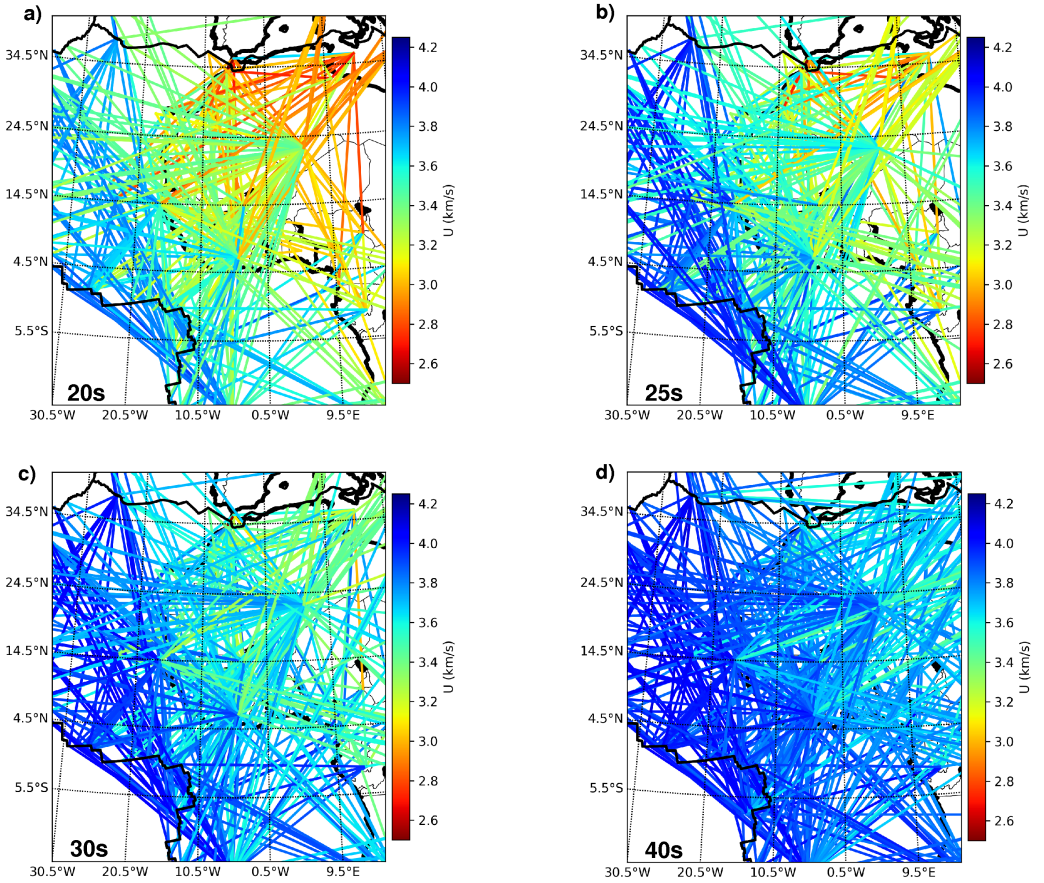

Fig. 9 Path coverage maps for group-velocity measurements at 20, 25, 30 and 40 s period. The color of each path is given by the corresponding group-velocity measurement.

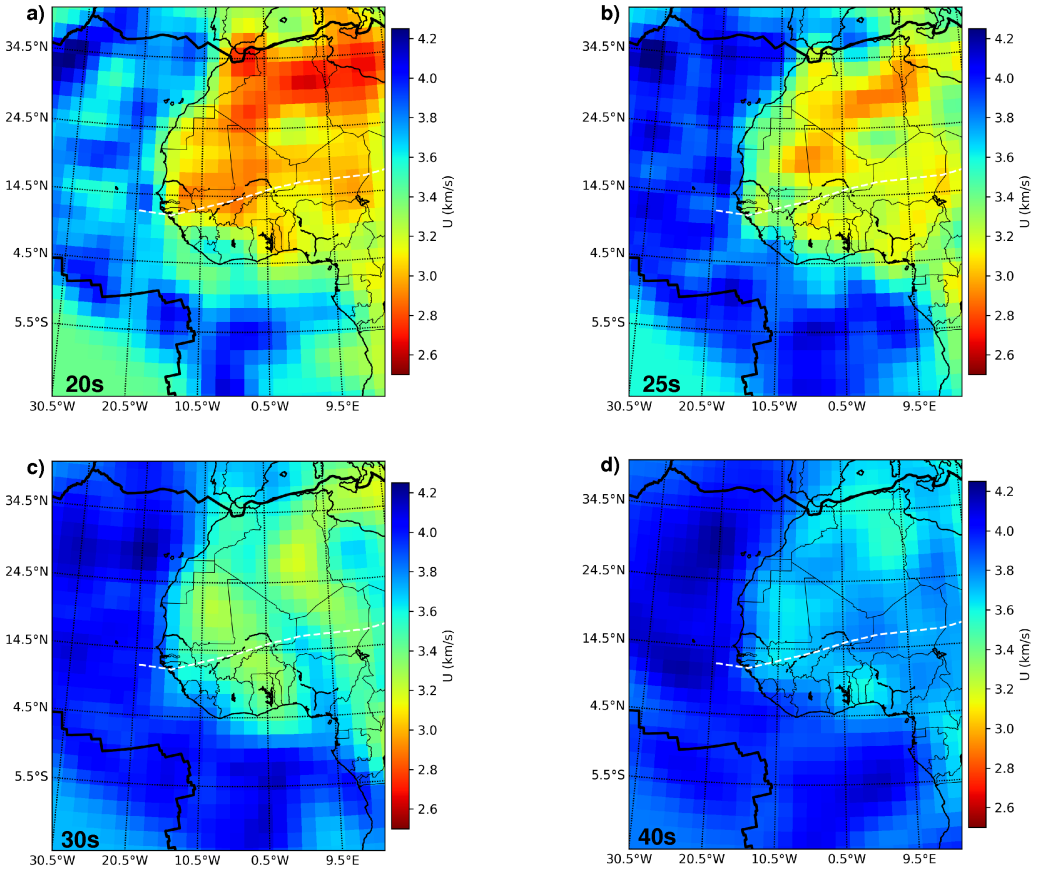

Fig. 10 Group-velocity maps for 20, 25, 30 and 40 s period, obtained by inverting the measurements shown in Figure 9. The colorscale indicates group-velocity. The white dashed line represents the Guinean-Nubian lineament (Guiraud et al., 2005). Black thick lines show the plate boundaries (Bird, 2003).

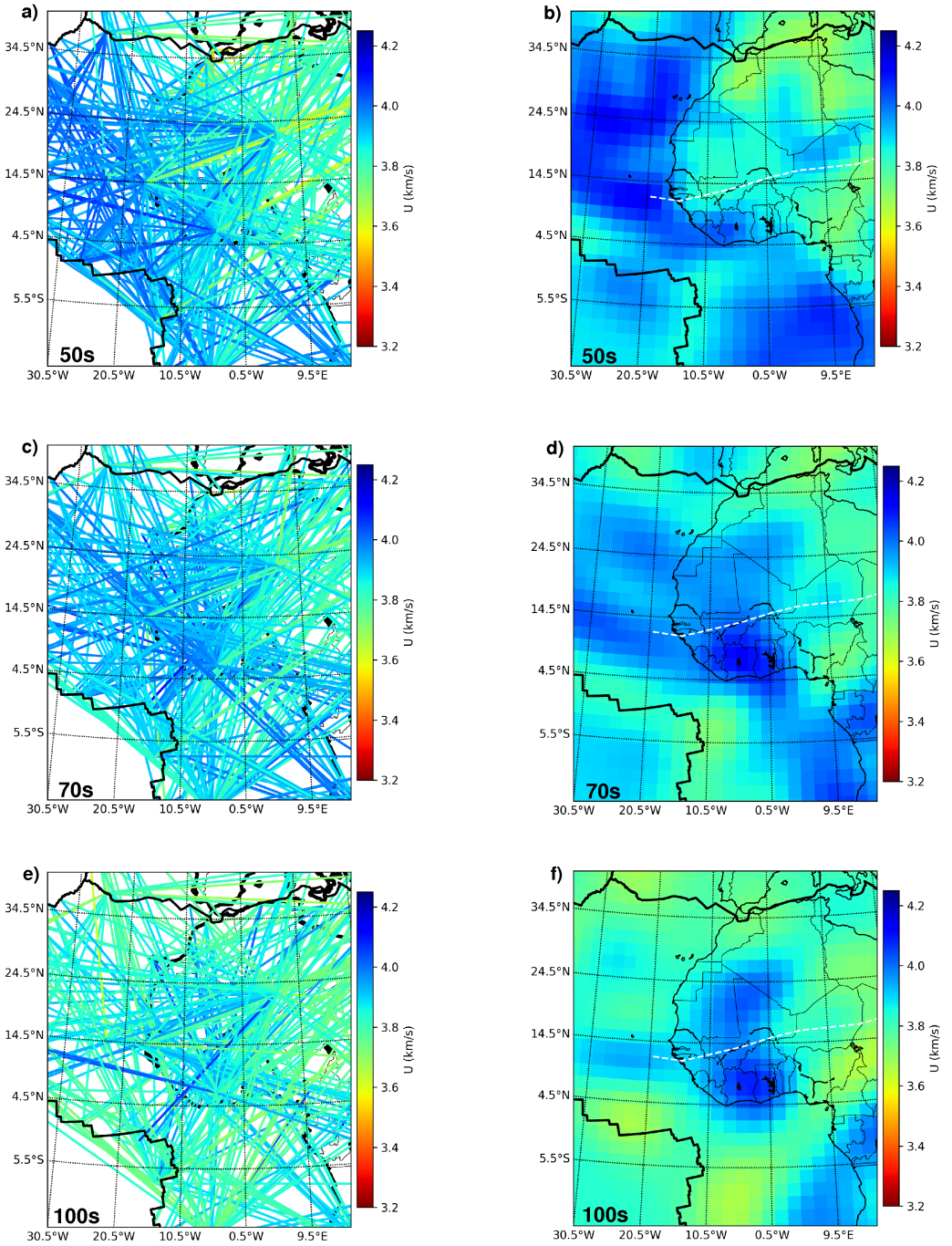

Fig. 11 Path coverage (a, c, e) and group-velocity maps (b, d, f) for 50, 70 and 100 s period. The colorscale indicates group-velocity. The white dashed line represents the Guinean-Nubian lineament (Guiraud et al., 2005). Black thick lines show the plate boundaries (Bird, 2003).

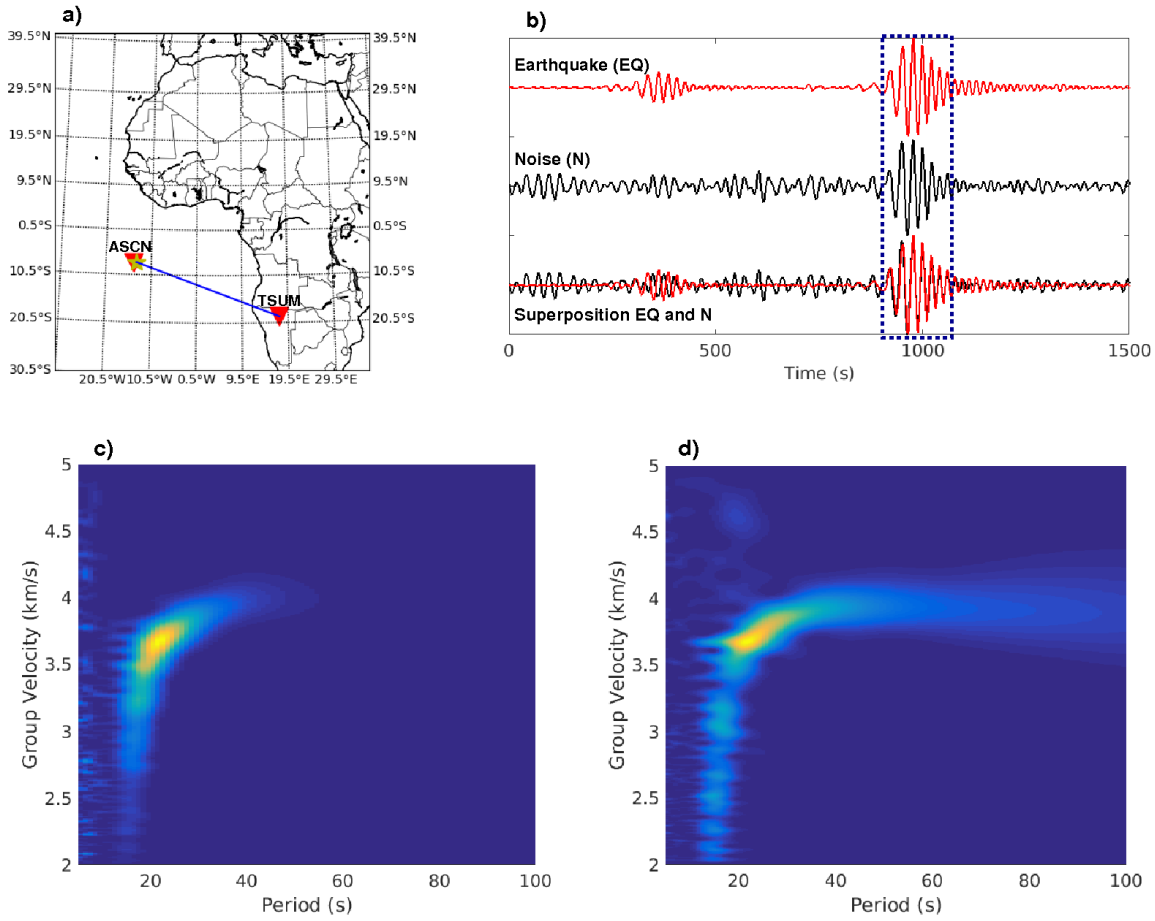

Fig. 12 Comparison of seismograms and dispersion curves from the 2000/06/16 Mw 5.0 earthquake (epicenter near ASCN station) recorded by TSUM station and the cross-correlation of seismic ambient noise between the station-pair ASCN-TSUM. The epicentral distance is 3609 km and inter-station distance is 3667 km; we corrected the earthquake waveform for the 58 km difference in distance assuming an average group velocity of 3.63 km/s and filtered the seismograms between 20 and 40 s. (a) Location of earthquake (yellow star) and stations (red triangles). (b) Filtered waveforms from the earthquake (red) and noise correlation (black); the blue rectangle indicates the surface wave packets. (c) and (d) Dispersion diagram of the earthquake and seismic ambient noise cross-correlation respectively.

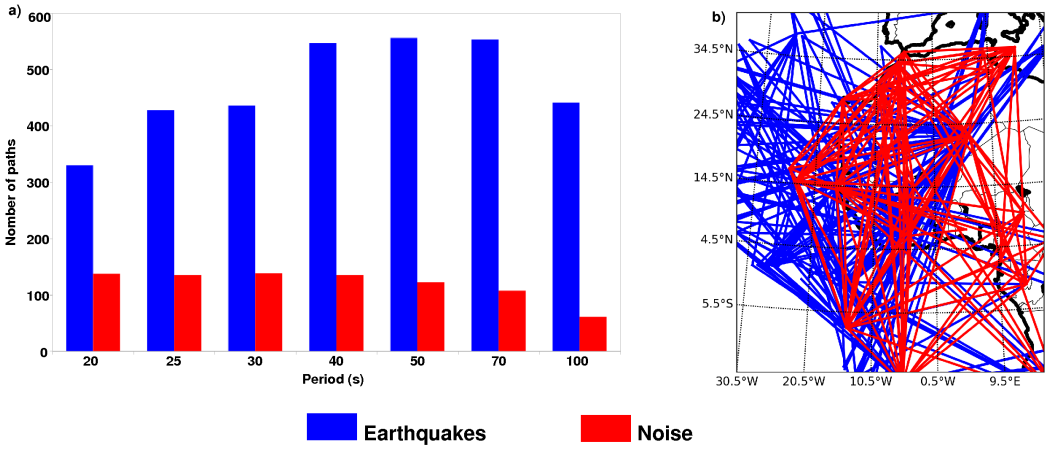

Fig. 13 (a) Number of group-velocity measurements at each period obtained from earthquakes (blue) and ambient noise correlations (red). (b) Path coverage at 20 s period.

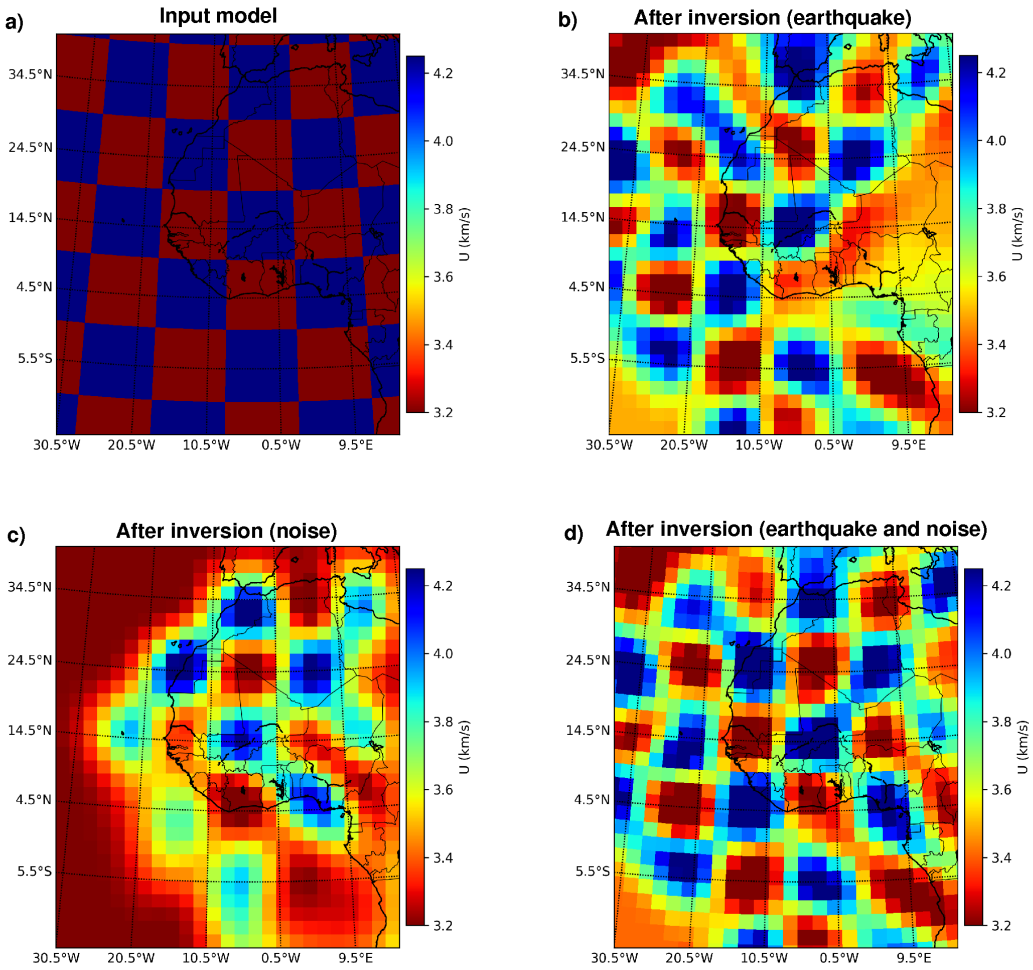

Fig. 14 Checkerboard tests for horizontal resolution with $10° \times 10°$ horizontal anomalies. (a) Input model. (b), (c), and (d) Models after inversion using: (b) only earthquake measurements; (c) only noise measurements; (d) both earthquake and noise measurements.

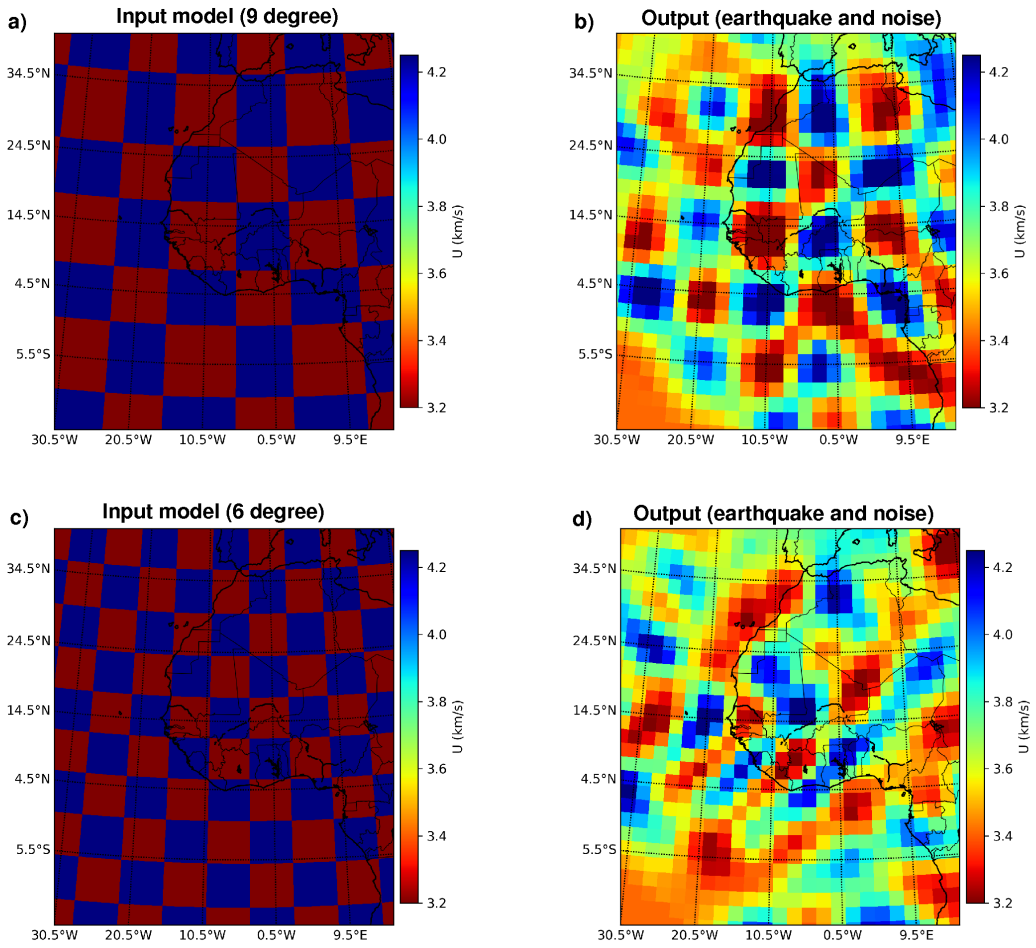

Fig. 15 Checkerboard tests for 9° × 9° and 6° × 6° using the full path distribution and measurement uncertainties at 20 s. (a) and (c) Synthetic input models for 9 degrees and 6 degrees. (b) and (d) Output models corresponding to (a) and (c).